Three-Dimensional Modeling of 900-MHz and 2.44-GHz Radio Propagation in Corridors

J. H. Tarng, W. R. Chang, and B. J. Hsu

***Abstract*—A three-dimensional (3-D) propagation model, combined with a patched-wall model, has been developed to predict radio loss in a corridor environment. The ray-tracing technique is used and combined with the ray-fixed coordinate system to simplify the computations of transmission, reflection, and diffraction coefficients in 3-D space. The computed path loss is compared with the measured value of 900-MHz and 2.44-GHz radio propagation along a hallway and gives a reasonable agreement. It is also found that the fields transmitted through the interior walls give the major contribution to the received field when the radio path lies around a corner.**

***Index Terms*—Field strength measurement, indoor radio propagation, Raytracing technique.**

I. Introduction

RADIO propagation in the UHF band has been proposed as a basis for radio local-area networks (R-LAN's) and personal communications services (PCS's) [1], [2]. These systems such as DECT, CT2, CT3, and the universal portable digital communications (UPDC) in the United States can find important applications inside large office buildings. Their implementation requires an understanding of the radio propagation characteristics of the signal inside such structures. Knowing the radio coverage inside the building, the allocation of base stations can be determined.

Inside buildings, radio waves may experience reflection, refraction, diffraction, and scattering by in-building structures. Due to these effects, the transmitted signal most often arrives at receivers by more than one path. It results in a phenomenon known as multipath fading [3]–[5]. The multiple paths at the receivers, including indirect paths and a direct path (if it exists), interfere with one another. In narrow-band transmission, the multipath propagation yields both amplitude and phase fluctuations of the received field. In wide-band pulse transmission, the effect is to produce a series delayed and attenuated echoes for each transmitted pulse. In this research, the major effort is focused on narrow-band (900-MHz and 2.44-GHz) propagation. Although the physical indoor radio environment is very complicated, there have been a number of recent studies of indoor radio propagation modeling [6]–[14] because of its practical importance. This research has developed both empirically based statistical [6]–[10] and theoretical models [11]–[14].

In [11], the authors have shown that there are two significant geometric features, which are the clear space between the ceiling and furnishings or floor and reflection and transmission at the interior and exterior walls that govern the propagation on single floors in modern office buildings. They used absorbing screens to calculate the excess loss in office and hallway environments. In [12], Seidel and Rappaport have developed a site-specific model by using the ray-tracing method to predict propagation based on a building blueprint representation. The concept of effective building material properties is developed. The prediction is made in hallway environments with standard deviation of error-of-path loss being around 5 dB. In [13], the authors have proposed an idealized model in dealing with the corridor environment. In [14], the authors have shown that a circular polarized wave for line-of-sight (LOS) indoor radio communications can significantly mitigate the multipath fading. This research reveals that the radio propagation in the corridor environment and polarization of the radio are both important research subjects in indoor propagation modeling.

In this study, a three-dimensional (3-D) propagation model, combined with a patched-wall model, has been developed and applied to predict 900-MHz and 2.44-GHz radio propagation in a corridor environment with inclusion of polarization. There are few papers dealing with 3-D propagation modeling in an indoor environment. The model employs ray-fixed coordinate systems and electromagnetic theory to predict both the polarization and field strength of the received vector field. The ray-fixed coordinate is a local coordinate system whose coordinate-axes are determined by the direction of the incident (reflected) ray and the normal unit vector of the reflecting boundary. With this local coordinate, the calculation of the reflection, transmission, or even diffraction coefficient of the propagating radio wave is simplified, which saves a lot of computer simulation time. In addition, the patched-wall model can represent the physical radio environment properly. By incorporating these two additional new treatments into the ray-tracing technique, both the prediction accuracy and saving of simulation time can be reasonably improved. Here, the model is verified to predict 900-MHz and 2.44-GHz radio propagation along a hallway and around a corner. The side walls of the corridor are modeled by patches of different dielectrics. The computed results are validated by the experimental results, and the propagation mechanisms in these two environments are explored.

Manuscript received February 14, 1996; revised May 3, 1996. This work was supported by the National Science Council of Taiwan under Projects NSC85-2221-E-009-035 and NSC83-0404-E009-090.

The authors are with the Department of Communication Engineering, National Chiao Tung University, Hsin-Chu, Taiwan, R.O.C.

Publisher Item Identifier S 0018-9545(97)03134-4.

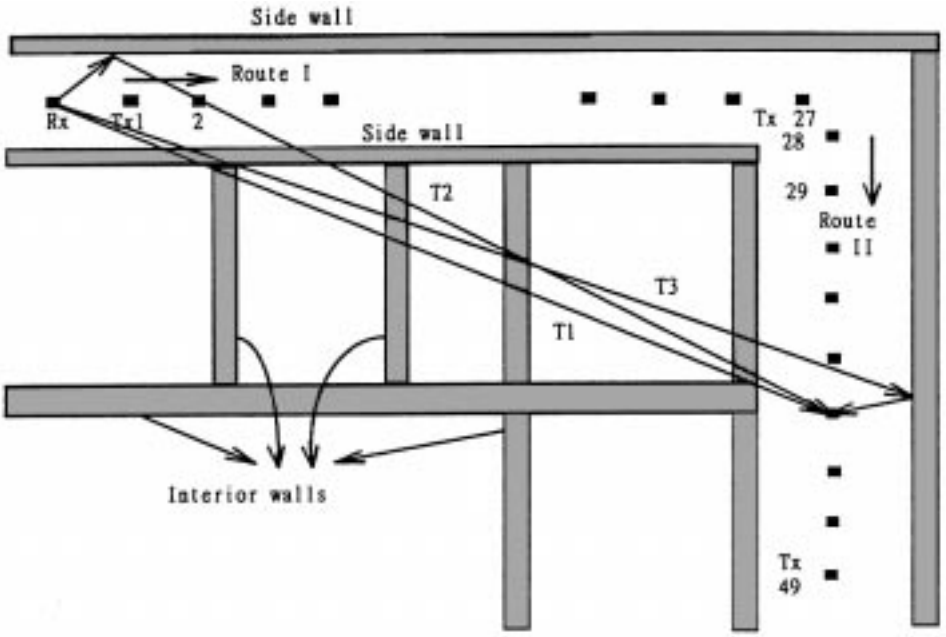

Fig. 1. Layout of measurement site of the floor. Rx and Tx represent the positions of the receiver and transmitter, respectively. There are 27 measured positions for Route I (Tx 1–Tx 27) and 22 measured positions for Route II (Tx 28–Tx 49).

The rest of this paper is organized as follows. The measurement setup and propagation environment are described in Section II. In Section III, formulations of reflection, transmission, and diffraction coefficients are delivered in the ray-fixed coordinate systems. The 3-D propagation model, combined with the patched-wall model, is developed in Section IV. The comparison between the computed and experimental results is also illustrated in Section IV. Conclusions are discussed in the last section.

II. Propagation Environment and Experimental Setup

A. Propagation Environment and Patched-Wall Model

The measurement site shown in Fig. 1 is at the ninth floor of the Engineering Building Four at the National Chiao-Tung University, Hsin-Chu, Taiwan, R.O.C. Measurements of 900-MHz and 2.44-GHz propagation loss have been conducted in a corridor. Two measurement routes are designed to reflect the major geometric features of the corridor. There are paths along the hallway (Route I) and around the corner (Route II), as shown in Fig. 1. The width, height, and length of the hallway are 2.6, 2.4, and 34 m, respectively. The floor of the corridor is made of concrete. The major feature of the ceiling is defined by the lighting fixtures made of metal. The side walls are mainly made of plasterboard. However, some sectors of the walls of the corridor are made of different materials, for example, wood, metal, concrete, or even glass, which will yield different reflectivity of the incident wave. Neglecting the difference of reflectivity will degrade predicting accuracy of the propagation model. Therefore, in [12], the authors have proposed the concept of an "effective building material" to reflect the physical and complicated constitutive materials of the building walls. However, permittivity of the effective material is not easy to determine since it depends on the experimental data as well as the propagation model. To simplify this problem, we introduce patches of different dielectric constants and physical sizes to represent the physical walls. It is called the patched-wall model. In Fig. 2, five different patches with different sizes are used to represent the side walls of the hallway since the side walls are made of five different materials. It is noted that the size and dielectric constant of each patch are chosen according to its physical dimension and the material it is made of.

B. Measurement Setup and Procedure

Narrow-band (CW) signal-strength measurements were made at 900 MHz and 2.44 GHz. A 0- or 15-dBm CW signal was transmitted by a half-wavelength dipole antenna at a height of 1.6 m above the floor. The transmitted signal is also received by a half-wavelength dipole antenna with a 1.2-m height. The receiver (Advantest R3261A) can instantaneously measure the signal strength between 10 dBm to -90 dBm over a 10-KHz bandwidth for 900 MHz and over a 100-KHz bandwidth for 2.44 GHz. The transmitting system has been calibrated in an anechoic chamber. During the measurement along the hallway (Route I), the transmitting antenna is moved from position 1 to 27, while the receiving antenna is stationary. For measurement around the corner (along Route II), 22 measured points are conducted. At each measured point, the measured field strength is obtained by a spatial sector average over nine grid subpoints with a quarter-wavelength spacing between neighboring points. To assure that the propagation channel is time stationary, the measured data has been averaged on screen over ten instantaneous sampled values. Here, both antennas may have different polarizations.

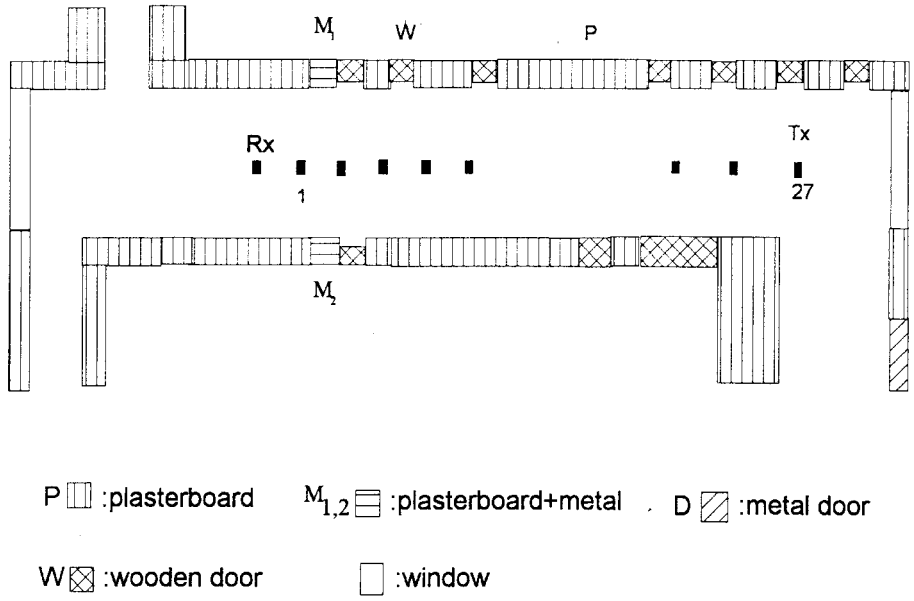

Fig. 2. Patched-wall model of the corridor. There are five different patches.

III. Reflection, Transmission, and Diffraction Coefficients

The formulations of reflection, transmission, and diffraction coefficients of different polarizations are given in this section since they will be used in our model to compute the indoor path loss. Because a 3-D model is constructed and polarizations of the electric field are considered, a ray-fixed coordinate system is introduced to simplify the calculations of these coefficients.

A. Ray-Fixed Coordinate Systems

Tracing rays in 3-D space in a building, including the polarization of the field using a global coordinate system, requires that the transmission, reflection, or diffraction coefficients of the propagating field must be represented by 3×3 matrices. The components of the matrix sometimes are difficult and time-consuming to determine. When a ray-fixed coordinate system is used, the matrix reduces to a 2×2, which is much easier to determine.

An example of a wave reflected at a boundary is demonstrated to describe how to apply the ray-fixed coordinate to calculate the reflected field. In Fig. 3, one ray emitting from point source S intersects a boundary at position R, where it is reflected. Position F is the observation point along the reflected ray. The length of segments SR and RF are denoted by S_1 and S_2, respectively.

The reflected field $\vec{E}_R^r(x, y, z)$ at position R is determined by the incident field $\vec{E}_R^i(x, y, z)$ at position R by the relation

$$\vec{E}_R^r(x, y, z) = \overline{\overline{R}} \cdot \vec{E}_R^i(x, y, z) \tag{1}$$

where $\overline{\overline{R}}$ is called the reflection matrix and is a 3×3 matrix in the global coordinate system (x, y, z). In Fig. 2, the incident and reflected ray-fixed coordinates, represented by $(\hat{s}_1, \hat{\alpha}_1, \hat{\beta}_1)$ and $(\hat{s}_2, \hat{\alpha}_2, \hat{\beta}_2)$, respectively, are introduced to reduce the number of matrix elements. $\hat{s}_1$ is the incident unit vector along the direction from source point S to reflection point R. $\hat{s}_2$ is the reflected unit vector along the direction from point R to point F. $\hat{n}$ is the normal unit vector of the boundary. Here, $\hat{\alpha}_i$ and $\hat{\beta}_i$, $i = 1, 2$, are defined by

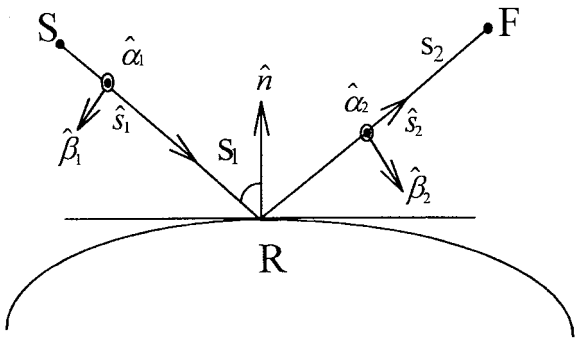

Fig. 3. The ray-fixed coordinate system associated with the reflection at the boundary.

$$\hat{\alpha}_1 = \frac{\hat{s}_1 \times \hat{n}}{|\hat{s}_1 \times \hat{n}|}$$
$$\hat{\beta}_1 = \frac{\hat{s}_1 \times \hat{\alpha}_1}{|\hat{s}_1 \times \hat{\alpha}_1|} \tag{2}$$
$$\hat{\alpha}_2 = \frac{\hat{s}_2 \times \hat{n}}{|\hat{s}_2 \times \hat{n}|}$$
$$\hat{\beta}_2 = \frac{\hat{s}_2 \times \hat{\alpha}_2}{|\hat{s}_2 \times \hat{\alpha}_2|}. \tag{3}$$

Vectors $\hat{\beta}_1$ and $\hat{\beta}_2$ are unit vectors in the incident (reflected) plane. In the $(\hat{s}_1, \hat{\alpha}_1, \hat{\beta}_1)$ and $(\hat{s}_2, \hat{\alpha}_2, \hat{\beta}_2)$ coordinate systems, $\vec{E}_R^i(x, y, z)$ and $\vec{E}_R^r(x, y, z)$ are expressed by $(E_{\alpha_1}^i, E_{\beta_1}^i, E_{s_1}^i)$ and $(E_{\alpha_2}^i, E_{\beta_2}^i, E_{s_2}^i)$, respectively. With these two coordinates, the component of the incident and

reflected waves along the ray direction becomes zero, i.e., $E^i_{s_1} = E^r_{s_2} = 0$. Therefore, the functions in (1) can be reduced to

$$\vec{E}^i_R(x, y, z) = \hat{\alpha}_1 E^i_{\alpha_1} + \hat{\beta}_1 E^i_{\beta_1} = \begin{pmatrix} E^i_{\alpha_1} \\ E^i_{\beta_1} \end{pmatrix} \tag{4}$$

$$\vec{E}^r_R(x, y, z) = \hat{\alpha}_2 E^r_{\alpha_2} + \hat{\beta}_2 E^r_{\beta_2} = \begin{pmatrix} E^r_{\alpha_2} \\ E^r_{\beta_2} \end{pmatrix} \tag{5}$$

$$\overline{\overline{R}} = \begin{pmatrix} R_{\alpha\alpha} & R_{\alpha\beta} \\ R_{\beta\alpha} & R_{\beta\beta} \end{pmatrix} \tag{6}$$

where $R_{\alpha\alpha} = R_s$, $R_{\beta\beta} = R_p$, and $R_{\alpha\beta} = R_{\beta\alpha} = 0$.

Here R_s and R_p are reflection coefficients of perpendicular and parallel polarizations, respectively, and are given by [15]

$$R_s = \frac{\eta_2 \cos\theta_i - \eta_1 \cos\theta_t}{\eta_2 \cos\theta_i + \eta_1 \cos\theta_t}$$
$$R_p = \frac{\eta_1 \cos\theta_i - \eta_2 \cos\theta_t}{\eta_1 \cos\theta_i + \eta_2 \cos\theta_t} \tag{7}$$

where η_1 and η_2 are the intrinsic impedance of the medium one and two, respectively. The transmission coefficients of perpendicular and parallel polarizations, represented by T_s and T_p, respectively, are given by

$$T_s = \frac{2\eta_2 \cos\theta_i}{\eta_1 \cos\theta_t + \eta_2 \cos\theta_i}$$
$$T_p = \frac{2\eta_2 \cos\theta_i}{\eta_1 \cos\theta_i + \eta_2 \cos\theta_t}. \tag{8}$$

It is noted that

$$\cos\theta_t = \left[1 - \left(\frac{\eta_2}{\eta_1}\right)^2 \sin^2\theta_i\right]^{1/2} \tag{9}$$

where θ_i and θ_t are the angles of incidence and refraction, respectively.

In the physical world, the structure of the building wall is layered. Therefore, a layered structure is considered in the computation of the transmission coefficients in our model. By treating each layer as a segment of the transmission line with a corresponding impedance, the transmission and reflection coefficients of the layered structure are calculated by the $ABCD$ matrix and given by [15]

$$R_{s,p} = \frac{A + \frac{B}{Z_t} - Z_1\left(C + \frac{D}{Z_t}\right)}{A + \frac{B}{Z_t} + Z_1\left(C + \frac{D}{Z_t}\right)} \tag{10}$$

$$T_{s,p} = \frac{2}{A + \frac{B}{Z_t} + Z_1\left(C + \frac{D}{Z_t}\right)} \tag{11}$$

where the subscripts of s and p represent the incident wave with s and p polarizations, respectively. Here, the ray-fixed coordinate system is used.

The notations A, B, C, and D are given by

$$\begin{pmatrix} A & B \\ C & D \end{pmatrix} = \begin{pmatrix} A_1 & B_1 \\ C_1 & D_1 \end{pmatrix}\begin{pmatrix} A_2 & B_2 \\ C_2 & D_2 \end{pmatrix}\cdots\begin{pmatrix} A_N & B_N \\ C_N & D_N \end{pmatrix}. \tag{12}$$

Coefficients in each matrix on the right-hand side of the equation above are determined by the dielectric constant, permeability, layered thickness, and refractive angle of the corresponding layer. For example, for layer m

$$A_m = D_m = \cos q_m l_m,$$
$$B_m = jZ_m \sin q_m l_m, \qquad (m = 1, \cdots, N) \tag{13}$$
$$C_m = \frac{j \sin q_m l_m}{Z_m}, \qquad A_m D_m - B_m C_m = 1 \tag{14}$$
$$q_m = k_m \cos\theta_m = k_m\left[1 - \left(\frac{n_1}{n_m}\right)^2 \sin^2\theta_i\right]^{1/2}$$
$$k_m = k_0 \cdot n_m \tag{15}$$

where θ_m is the refractive angle. Notation l_m is the layer thickness, and n_m is the index of refraction. It is given that

$$q_i = k_1 \cos\theta_i$$
$$q_t = k_t \cos\theta_t \tag{16}$$

and θ_i and θ_t are the angles of incidence and refraction, respectively.

It is noted that $Z_m = \omega\mu_m/q_m$ for s polarization and $Z_m = q_m/\omega\epsilon_m$ for p polarization.

B. Diffraction Around Corners

The uniform theory of diffraction is employed to calculate the diffraction field of the corner in the corridor. In Fig. 4, a conducting wedge with angle $(2 - n)\pi$ is illustrated for oblique incidence. Under the assumption that the wedge is extended infinite along the z direction, the diffracted E-field components, which are parallel $(E^d_{\beta_2})$ and perpendicular $(E^d_{\alpha_2})$ to the plane of diffraction (the shaded region in Fig. 4), is given by [16]

$$\begin{bmatrix} E^d_{\beta_2}(s_2) \\ E^d_{\alpha_2}(s_2) \end{bmatrix} = -\begin{pmatrix} D_s & 0 \\ 0 & D_h \end{pmatrix}\begin{bmatrix} E^i_{\beta_1}(D) \\ E^i_{\alpha_1}(D) \end{bmatrix} \cdot A(s_1, s_2)e^{-jks_2} \tag{17}$$

where D_s and D_h are the diffraction coefficients of the soft and hard polarization, respectively, and given by

$$D_{s,h} = \frac{1}{\sin\beta_1}(\{d^+(\alpha^-)F[kLg^+(\alpha^-)] + d^-(\alpha^-)F[kLg^-(\alpha^-)]\} \mp \{d^+(\alpha^+)F[kLg^+(\alpha^+)] + d^-(\alpha^+)F[kLg^-(\alpha^+)]\}) \tag{18}$$

with D_s corresponding to the negative sign. Here, $d^{\pm}(\alpha)$ is defined by

$$d^{\pm}(\alpha) = -\frac{e^{(j\pi/4)}}{2n\sqrt{2\pi k}} \cot\left(\frac{\pi \pm \alpha}{2n}\right) \tag{19}$$

and $F(x)$ is known as the transition function given by

$$F(\xi) = 2j\sqrt{\xi}\exp(j\xi)\int_{|\xi|}^{\infty} e^{-j\tau^2}\, d\tau. \tag{20}$$

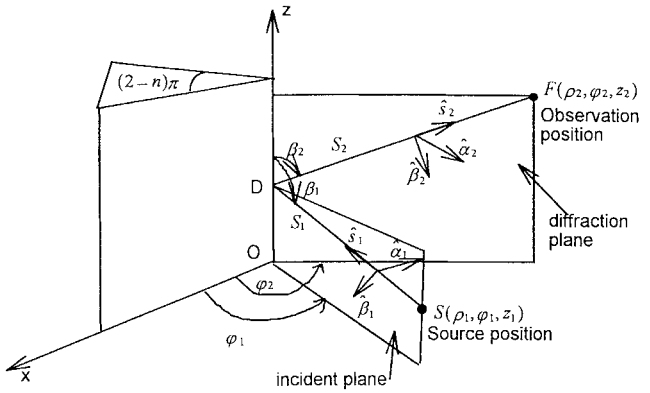

Fig. 4. Geometry of a 3-D diffraction by a conducting wedge with angle $(2-n)\pi$ for oblique incidence.

The argument of the transition function, which is $\xi = kLg(\alpha)$, k is the wave number, and L, a distance parameter, is dependent on the form of incident wave and given by

$$L = \begin{cases} s_2 \sin^2 \beta_1 & \text{plane wave incidence} \\ \dfrac{\rho_1 \rho_2}{\rho_1 + \rho_2} & \text{cylindrical wave incidence} \\ \dfrac{s_1 s_2}{s_1 + s_2} \sin^2 \beta_1 & \text{spherical wave incidence.} \end{cases} \tag{21}$$

The function $g(\alpha)$ is defined as

$$g^{\pm}(\alpha) = 1 + \cos(\alpha - 2nN^{\pm}\pi) \tag{22}$$

where $N^+ = (1/2n\pi)(\alpha^{\pm} + \pi)$ and $N^- = (1/2n\pi)(\alpha^{\pm} - \pi)$, with N^+ or N^- being a positive or negative integer or zero—whichever most closely satisfies the equation, and $\alpha^- = \phi_2 - \phi_1$, $\alpha^+ = \phi_2 + \phi_1$, where ϕ_1 and ϕ_2 are the components of (ρ_1, ϕ_1, z_1) and (ρ_2, ϕ_2, z_2), which are the source and receiver positions, respectively, in the cylindrical coordinate system. Here, the z-axis of the cylindrical coordinate system is along the edge of the wedge.

The spatial attenuation factor $A(s', s)$, which describes how the field intensity varies along the diffracted ray, is given by

$$A(s_1, s_2) = \begin{cases} \dfrac{1}{\sqrt{s_2}} & \text{plane, cylindrical wave incidence} \\ \sqrt{\dfrac{s_1}{s_2(s_1 + s_2)}} & \text{spherical wave incidence.} \end{cases} \tag{23}$$

Fermat's principle is employed to locate the point of diffraction of the edge. The position of the point is given by [16]

$$(x, y, z) = \left[0, 0, z_1 + (z_2 - z_1)\frac{\rho_1}{\rho_1 + \rho_2}\right] \tag{24}$$

where (ρ_1, ϕ_1, z_1) and (ρ_2, ϕ_2, z_2) are the source and receiver positions, respectively, in the cylindrical coordinate system.

IV. Propagation Models and Numerical Simulations

The principle of geometric optics is widely used to investigate the radio propagation in the complicated in-building environment, for wireless communications applications [11], [12], even though its applicability is confined to the high-frequency region. This is because geometric optics are easy to implement and more numerically efficient than low- and intermediate-frequency scattering methods. In our model, the geometric optic method is also used to trace significant direct (if it exists), reflected, transmitted, and refracted rays by which the field radiated by the source reached specified receiver locations. Singly diffracted fields are also computed.

A. Ray-Tracing Technique

Ray tubes are introduced to segment the transmission over the unit sphere. Each ray tube, chosen to have nearly equal shape and area, is represented by a source ray during the tracing process. Ray tracing is accomplished by an exhaustive search of a ray tree accounting for the decomposition of the ray at each building-object intersection. First, the algorithm determines if a LOS path exists. Next, it traces a source ray that is not the LOS path and detects if it intersects an object. If no intersection is found, the process stops and a new source ray is initiated. Once an intersection has occurred, it then checks to see if the ray from the intersection point directly to the receiver is received. If this ray is not received, the ray is identified as reflected and computed. This ray is then treated in a fashion similar to a source ray. Here, the transmitted rays are ignored. This recursion continues until the ray intensity falls below a specified threshold. The reception sphere [11], [12] is also used to determine whether the traced ray approaching a receiving point is received. The reception sphere radius is equal to $\alpha d/2$, where d is the unfolded total path length and α is the angular spacing between neighboring rays at the source.

B. Propagation Model

The models include direct, reflected, refracted, and diffracted fields that are represented by the rays. Each propagation mechanism is treated separately. The complex vector field of the ith ray at the receiver is given by

$$\vec{E}_i = \vec{E}_0 \cdot G_{ti} \cdot G_{ri} \cdot L_i(d) \cdot L_D(\phi_{1i}, \phi_{2i}) \prod_j \overline{\overline{R}}(\theta_{ji}) \tag{25}$$

where $\vec{E}_0$ is the vector field 1 m away from the transmitting antenna, G_{ti} and G_{ri} are the field amplitude radiation patterns of the transmitting and receiving antenna, and $L_i(d)$ is the free-space path loss of the ith component with an unfold total path length d. Here, $L_D(\phi_{1i}, \phi_{2i})$, calculated by (18), represents the diffraction loss of the ith ray. The reflection coefficients $\overline{\overline{R}}(\theta_{ji})$ are calculated by using (7)–(9) with incident angle θ_{ji}.

It is noted that we have neglected the contribution of the scattered field. This is because, most of time, its magnitude is smaller than that of the specular reflection field.

C. Numerical Simulations and Comparisons

In the numerical simulation made with the models, a total of 1800 source rays are generated and traced. It takes less than 1 min when computing the field at one receiving point on a PC586-90. The dielectric constants of the patches, as shown in Fig. 2, are chosen to equal 5.0 for the wooden door, 2.4 for

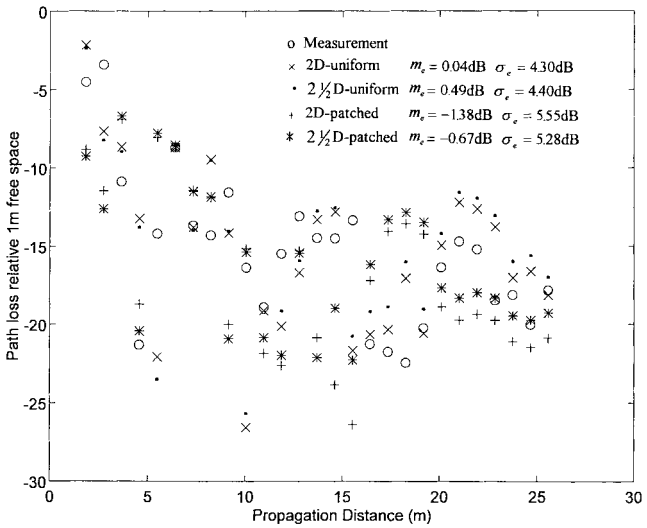

Fig. 5. The measured and predicted path losses of the 900-MHz radio wave as a function of propagation distance. The transmitting and receiving antennas are both vertically polarized.

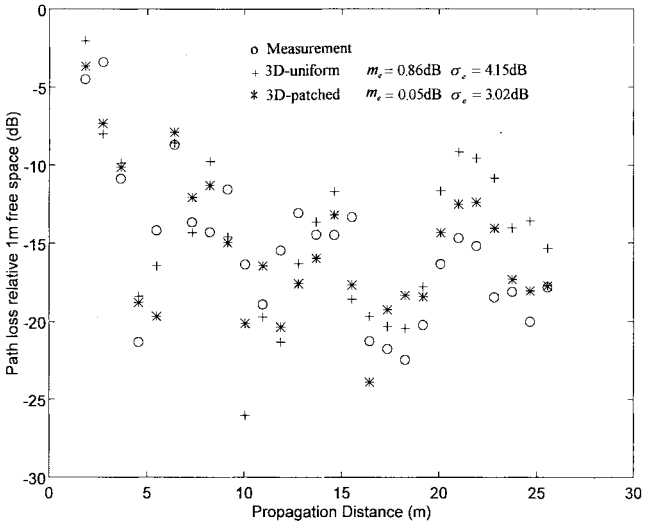

Fig. 6. The measured and predicted path losses of the 900-MHz radio wave as a function of propagation distance.

the window [17], and 2.0 for the ceiling at both propagating frequencies. Since the major feature of the ceiling is defined by the lighting fixtures made of metal, the reflection by the ceiling can be treated as diffused scattering to be neglected. However, to improve the prediction accuracy, the concept of effective material [12] is used here to determine the effective dielectric constant of the ceiling from our experimental data. For the plasterboard and concrete walls, the dielectric constants are chosen to equal 9.0–j2.0 and 9.0–j0.74 for 900 MHz and 2.44 GHz [17], respectively. In the case of propagation along the hallway, two-dimensional (2-D), two and one-half-dimensional ($2\frac{1}{2}$-D), and 3-D models are simulated and compared with one another. Here, the 2-D model only traces the reflected rays at the side walls, and the $2\frac{1}{2}$-D model includes not only the reflected rays from the side walls, but also the singly reflected rays from the ground and ceiling. In

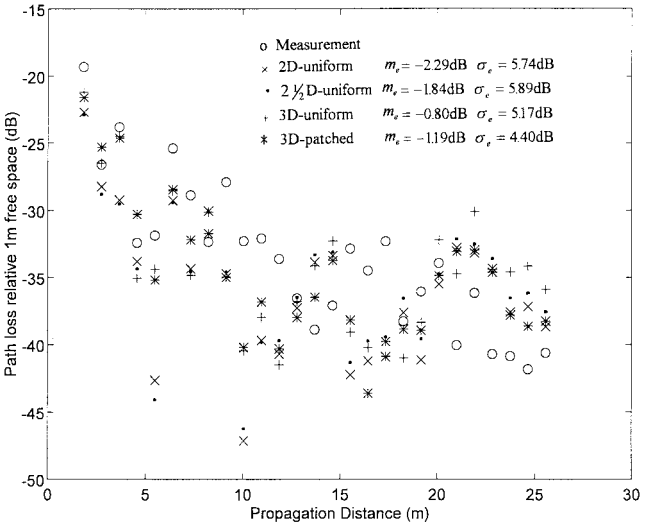

Fig. 7. The measured and predicted path losses of the 900-MHz radio wave as a function of propagation distance. The transmitting and receiving antennas are vertically and horizontally polarized, respectively.

the 2-D and $2\frac{1}{2}$-D models, the polarizations of the radio wave cannot be computed, but it is computed in the 3-D model.

1) Propagation Along the Hallway: In Fig. 5, the 900-MHz path losses computed by four models are compared with the experimental result measured along Route I, as shown in Fig. 1, with both the transmitting and receiving antennas being vertically polarized. The predictions employ 2-D uniform, 2-D patched, $2\frac{1}{2}$-D uniform, and $2\frac{1}{2}$-D patched models. The propagation model, combined with the patched-wall model as shown in Fig. 2, is called the "patched" model. Uniform means that the permittivity of the side walls is uniformly distributed. Both $2\frac{1}{2}$-D models give better prediction accuracy than that of the 2-D models, as is seen by comparing the values of m_e and σ_e, where m_e represents the mean error (the difference between the simulated and measured path losses) and σ_e is the standard deviation of the error. These models have a larger prediction error when the propagation distance is increased. In Fig. 6, the path losses computed by 3-D uniform and 3-D patched models are compared with the measured result. Both models give better prediction accuracy than those of the 2-D and $2\frac{1}{2}$-D models. Above all, the 3-D patched model has the best performance with $m_e = 0.05$ dB and $\sigma_e = 3.02$ dB.

When the polarization of the receiving antenna is changed to horizontal polarization, Fig. 7 shows the measured 900-MHz path loss and the computed result using the 2-D uniform, $2\frac{1}{2}$-D uniform, 3-D uniform, and 3-D patched models. The 3-D patched model still gives the best accuracy, with $m_e = -1.19$ dB and $\sigma_e = 4.40$ dB.

In the case of the 2.44-GHz radio wave propagating in the hallway, the measured path loss and the computed results for 2-D uniform, $2\frac{1}{2}$-D uniform, 3-D uniform, and 3-D patched models are illustrated in Fig. 8. Here, both the transmitting and receiving antennas are vertically polarized. The 3-D patched model still has the best prediction accuracy with $m_e = -2.77$ dB and $\sigma_e = 3.39$ dB. The measured and computed path losses are shown in Fig. 9 when the receiving antenna is changed to horizontal polarization. The 3-D patched model still gives the

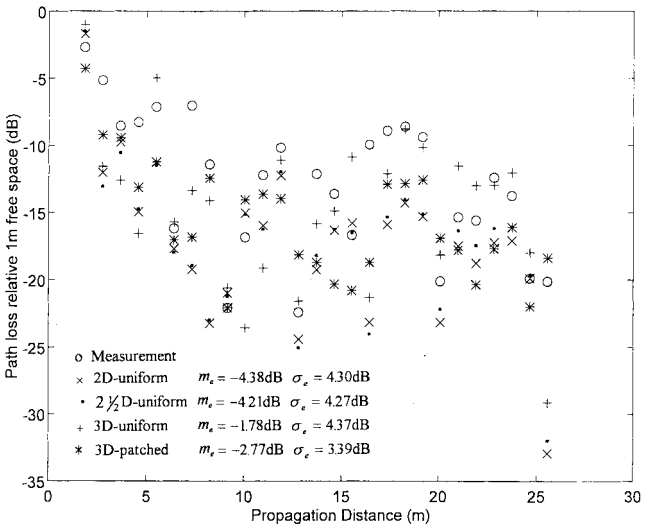

Fig. 8. The measured and predicted path losses of the 2.44-GHz radio wave as a function of propagation distance. The transmitting and receiving antennas are both vertically polarized.

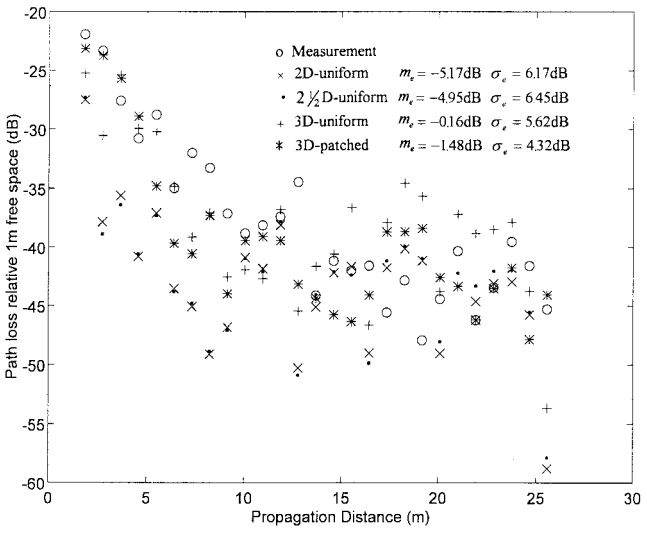

Fig. 9. The measured and predicted path losses of the 2.44-GHz radio wave as a function of propagation distance. The transmitting and receiving antennas are vertically and horizontally polarized, respectively.

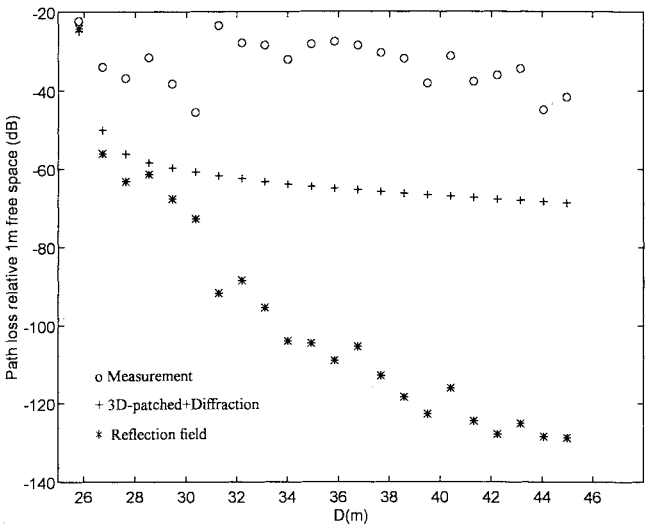

Fig. 10. The measured and computed path losses of 900-MHz radio propagation around the corner. The predicted patch loss is computed by the 3-D patched model with inclusion of a singly diffracted ray. The path loss computed by the 3-D patched model with the reflected rays only is also shown.

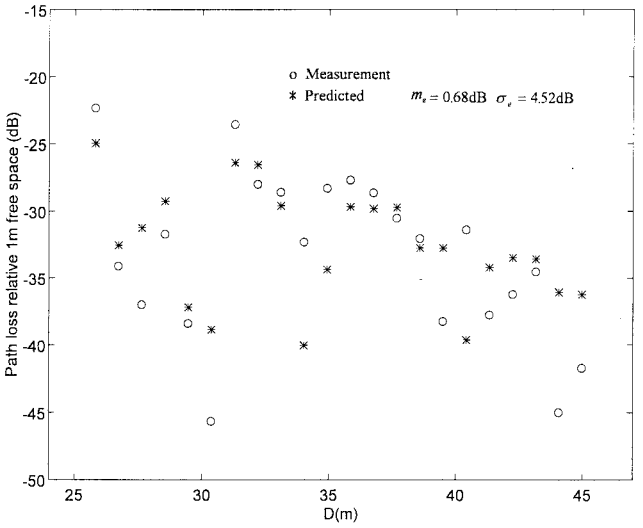

Fig. 11. The measured and predicted path losses of 900-MHz propagation around the corner. The predicted path loss is determined by the 3-D patched model with inclusion of the diffracted and transmitted rays.

best agreement with $m_e = -1.48$ dB and $\sigma_e = 4.32$ dB, while the other models give even worse prediction accuracy than in the previous case.

2) Propagation Around the Corner: Here, the 3-D patched model, combined with the singly diffracted ray, is employed to predict the path loss around the corner. In Fig. 10, the computed path loss is compared with the measured result along Route II (Tx 28–Tx 49) in Fig. 1. The horizontal axis is the route distance D, which is the accumulated distance by summing the distance between the neighboring measured points. It is seen that the predicted path loss is much larger than that measured, except for the first point (Tx 28). By checking our simulation results, as shown in Fig. 10, it is found that the contribution from the reflected rays to the receiver is very small in the out-of-sight (OOS) situation. The magnitude of the received reflected field is even much smaller than that of the diffracted field by an order about 30 dB. This is because the reflected rays for the receiving positions far away from the corner have been reflected more than ten times before they are received. As for the receiving positions near the corner, although the received rays have fewer times of reflection, they still lead to a weak received field strength since the incident ray at some reflection positions is close to the normal incidence. Additional measurements in the OOS situation indicate that the fields transmitted along Routes T1, T2, and T3, shown in Fig. 1, should be included since the interior walls are plasterboards with weak attenuation. Therefore, the transmitting rays through interior walls are traced. In Fig. 11, the computed path loss around the corner is compared with the measurement result for the case of 900 MHz. The prediction accuracy is amazingly improved with

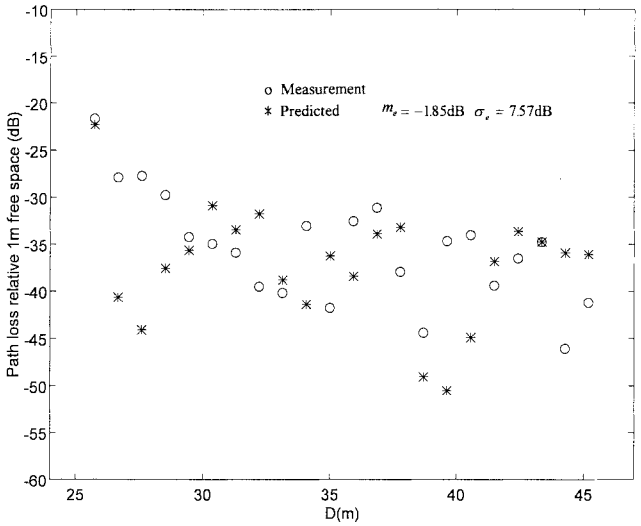

Fig. 12. The measured and predicted path losses of 2.44-GHz propagation around the corner. The predicted path loss is determined by the 3-D patched model with inclusion of the diffracted and transmitted rays.

TABLE I
THE VALUES OF m_e AND σ_e. HERE, U OR P REPRESENTS THE SIDEWALL TREATED AS A UNIFORM OR PATCHED ONE, RESPECTIVELY. VV POL. MEANS THAT BOTH THE TRANSMITTING AND RECEIVING ANTENNAS ARE VERTICALLY POLARIZED, AND VH POL. MEANS THAT THE RECEIVING ANTENNA IS HORIZONTALLY POLARIZED INSTEAD

	Model	900 MHz		2.44 GHz	
		VV Pol.	VH Pol.	VV Pol.	VH Pol.
m_e (dB)	2D-U	0.04	-2.29	-4.37	-5.12
	2½D-U	0.49	-1.84	-4.20	-4.95
	3D-U	0.86	-0.80	-1.78	-0.16
	3D-P	0.05	-1.19	-2.77	-1.48
σ_e (dB)	2D-U	4.30	5.74	4.30	6.17
	2½D-U	4.40	5.89	4.27	6.45
	3D-U	4.15	5.17	4.37	5.62
	3D-P	3.02	4.40	3.39	4.32

$m_e = 0.68$ dB and $\sigma_e = 4.52$ dB. For the case of 2.44 GHz, the computed path loss compared with the measured result has $m_e = -1.85$ dB and $\sigma_e = 7.57$ dB, as illustrated in Fig. 12, which is not so accurate. It is found that the first few predicting points have larger errors since the transmitted rays to these points propagate through the inside of the interior walls, where the structure and materials strongly affect the propagation.

V. CONCLUSION

In Table I, the values m_e and σ_e for 900-MHz and 2.44-GHz radio propagation in the hallway are listed for the patched and uniform models. Although the $2\frac{1}{2}$-D and 3-D uniform models provide a reasonable prediction accuracy in the 900-MHz case, they are poor at 2.44 GHz, especially in the VH polarization situation, which means that the transmitting and receiving antennas are vertically and horizontally polararized, respectively. It is because some small metallic objects are neglected, for example, the metallic frame of the window, metallic handles of the doors, and the metallic frame of ceiling. The objects may have larger effects on the 2.44-GHz radio wave since their size is comparable to the wavelength. The 3-D patched model, including the physical propagation environment, always gives the best and most consistent prediction accuracy. This model may also be useful for predicting radio waves in large offices with a proper choice of the reflecting boundary. When the radio path lies around a corner, the fields transmitted through the interior walls composed of plasterboards give the major contribution to the received field instead of the diffracted waves.

REFERENCES

[1] M. Marcus, "Regulatory policy considerations for radio local area networks," *IEEE Commun. Mag.*, vol. 25, no. 7, pp. 95–99, 1987.
[2] H. Hashemi, "The indoor radio propagation channel," *Proc. IEEE*, vol. 81, no. 7, pp. 943–968, 1993.
[3] T. S. Rappoport, "Characterization of UHF multipath radio channel in factory buildings," *IEEE Trans. Antennas Propagat.*, vol. 37, pp. 1058–1069, Aug. 1989.
[4] R. Bultitude, S. Mahmoud, and W. Sullivan, "A comparison of indoor radio propagation characteristics at 910 MHz and 1.75 GHz," *IEEE J. Select. Areas Commun.*, vol. 7, pp. 20–30, Jan. 1989.
[5] J. F. Lafortune and M. Lecours, "Measurement and modeling of propagation losses in a building at 900 MHz," *IEEE Trans. Veh. Technol.*, vol. 39, no. 2, pp. 101–108, 1990.
[6] S. Y. Seidel and T. S. Rappaport, "Path loss prediction in multifloored buildings at 914 MHz," *Electron. Lett.*, vol. 27, pp. 1384–1387, July 1991.
[7] ——, "914 MHz path loss prediction models for indoor wireless communications in multifloored buildings," *IEEE Trans. Antennas Propagat.*, vol. 40, pp. 207–217, Feb. 1992.
[8] A. J. Motley and J. M. P. Keenan, "Personal communication radio coverage in buildings at 900 MHz and 1700 MHz," *Electron. Lett.*, vol. 24, pp. 763–764, June 1988.
[9] A. J. Motley and J. M. P. Keenan, "Radio coverage in buildings," *Br. Telecom Technol. J., Special Issue Mobile Commun.*, vol. 8, pp. 19–24, 1990.
[10] D. Molkdar, "Review on radio propagation into and within buildings," *Proc. Inst. Elec. Eng.*, vol. 138, pt. H, pp. 61–73, Feb. 1991.
[11] W. Honcharenko, H. L. Bertoni, J. L. Dailing, J. Qian, and H. D. Yee, "Mechanisms governing UHF propagation on single floors in modern office buildings," *IEEE Trans. Veh. Technol.*, vol. 41, no. 4, pp. 496–504, 1992.
[12] S. Y. Seidel and T. S. Rappaport, "Site-specific propagation prediction for wireless in-building personal communication system design," *IEEE Trans. Veh. Technol.*, vol. 43, no. 4, pp. 879–892, 1994.
[13] G. M. Whitman, K. S. Kim, and E. Niver, "A theoretical model for radio signal attenuation inside buildings," *IEEE Trans. Veh. Technol.*, vol. 44, no. 3, pp. 621–629, 1995.
[14] A. Kajiwara, "Line-of-sight indoor radio communication using circular polarized waves," *IEEE Trans. Veh. Technol.*, vol. 44, no. 3, pp. 487–493, 1995.
[15] A. Ishimaru, *Electromagnetic Wave Propagation, Radiation, and Scattering.* Englewood Cliffs, NJ: Prentice-Hall, 1991.
[16] C. A. Balanis, *Antenna Theory—Analysis and Design.* New York: Wiley, 1982.
[17] M. C. Lawton and J. P. McGeehan, "The application of a deterministic ray launching algorithm for the prediction of radio channel characteristics in small-cell environments," *IEEE Trans. Veh. Technol.*, vol. 43, no. 4, pp. 955–969, 1994.

J. H. Tarng received the B.S. degree in power mechanical engineering from National Tsin-Hua University, Hsin-Chu, Taiwan, R.O.C., in 1981, and the M.S. and Ph.D. degrees in electrical engineering from Pennsylvania State University, University Park, in 1988 and 1989, respectively.

He is currently a Faculty Member in the Department of Communication Engineering, National Chiao Tung University, Hsin-Chu. His research interests include radio propagation modeling and measurement, indoor wireless communications, and ultrasonic scattering.

W. R. Chang received the B.S. and M.S. degrees in communication engineering from National Chiao-Tung University, Hsin-Chu, Taiwan, R.O.C., in 1994 and 1996, respectively. He is currently working toward the Ph.D. degree in the Department of Communication Engineering, National Chiao-Tung University, Hsin-Chu, Taiwan, R.O.C.

His research interest is in radio propagation modeling for indoor and microcellular communications.

B. J. Hsu received the B.S. degree in electron physics and the M.S. degree in communication engineering from National Chiao-Tung University, Hsin-Chu, Taiwan, R.O.C., in 1988 and 1995, respectively.

His research interests include wireless communication.